

Dynamical playground of a higher-order cubic Ginzburg-Landau equation: From orbital connections and limit cycles to invariant tori and the onset of chaos

V. Achilleos,¹ A. R. Bishop,² S. Diamantidis,³ D. J. Frantzeskakis,^{4,*} T. P. Horikis,⁵ N. I. Karachalios,³ and P. G. Kevrekidis^{2,6}

¹*Laboratoire d'Acoustique de l'Université du Maine, Avenue O. Messiaen, 72085 Le Mans, France*

²*Center for Nonlinear Studies and Theoretical Division, Los Alamos National Laboratory, Los Alamos, New Mexico 87545, USA*

³*Department of Mathematics, University of the Aegean, Karlovassi, 83200 Samos, Greece*

⁴*Department of Physics, University of Athens, Panepistimiopolis, Zografos, 15784 Athens, Greece*

⁵*Department of Mathematics, University of Ioannina, 45110 Ioannina, Greece*

⁶*Department of Mathematics and Statistics, University of Massachusetts, Amherst, Massachusetts 01003-4515, USA*

(Received 10 September 2015; published 11 July 2016)

The dynamical behavior of a higher-order cubic Ginzburg-Landau equation is found to include a wide range of scenarios due to the interplay of higher-order physically relevant terms. We find that the competition between the third-order dispersion and stimulated Raman scattering effects gives rise to rich dynamics: this extends from Poincaré-Bendixson-type scenarios, in the sense that bounded solutions may converge either to distinct equilibria via orbital connections or to space-time periodic solutions, to the emergence of almost periodic and chaotic behavior. One of our main results is that third-order dispersion has a dominant role in the development of such complex dynamics, since it can be chiefly responsible (even in the absence of other higher-order effects) for the existence of periodic, quasiperiodic, and chaotic spatiotemporal structures. Suitable low-dimensional phase-space diagnostics are devised and used to illustrate the different possibilities and identify their respective parametric intervals over multiple parameters of the model.

DOI: [10.1103/PhysRevE.94.012210](https://doi.org/10.1103/PhysRevE.94.012210)

I. INTRODUCTION

Nonlinear evolution equations are often associated with the theory of solitons and integrable systems [1]. A prime example is the nonlinear Schrödinger (NLS) equation, which constitutes one of the universal nonlinear evolution equations, with applications ranging from deep water waves to optics [2]. Remarkable phenomena are also exhibited by its higher-order variants, emerging in a diverse spectrum of applications, such as nonlinear optics [3], nonlinear metamaterials [4], and water waves of finite depth [5–7]. On the other hand, dissipative variants of NLS models incorporating gain and loss have also been used in optics [8], e.g., in the physics of mode-locked lasers [9,10] (see also the relevant works [11] and [12]) and polariton superfluids [13] (see, e.g., Ref. [14] for various applications). Note that such dissipative NLS models can be viewed as variants of the complex Ginzburg-Landau (CGL) equation, which has been extensively studied, especially in the context of pattern formation in far-from-equilibrium systems [15].

Dissipative nonlinear evolution equations (incorporating gain, loss, external driving, or combinations thereof) may exhibit (and potentially be attracted to) low-dimensional dynamical features, such as (a) one or more equilibria (and orbits connecting them), (b) periodic orbits, (c) quasiperiodic orbits, and (d) low-dimensional chaotic dynamics [16]. The availability of dynamical scenarios (a)-(d) depends on the effective dimensionality of the low-dimensional behavior; one-dimensionality only allows fixed points, planar systems governed by the Poincaré-Bendixson (PB) theorem [16] can also feature periodic orbits, and higher dimensions allow for quasiperiodic or chaotic dynamics. Various prototypical partial

differential equation models have demonstrated a PB-type behavior as an intermediate bifurcation stage in the route to spatiotemporal chaos. Examples include the Kuramoto-Sivashinsky [17] and CGL equations; regarding the latter, which is of primary interest in this work, we refer to the seminal works [18] for the spatiotemporal transition to chaos. In addition to the above autonomous systems, spatiotemporal chaos was also found in nonautonomous systems, due to the interplay between loss and external forces, such as the damped-driven NLS equation [19–21] (where the hyperbolic structure of the underlying integrable NLS equation is a prerequisite [22]) and the sine-Gordon [23] system.

In this work, we focus on the role of higher-order effects and investigate the possibility of bifurcation phenomena leading to the existence of the above prototypical examples of low-dimensional dynamics in an autonomous, physically important higher-order CGL-type model. This model is motivated by the higher-order NLS equation that is commonly used, e.g., in studies of ultrashort pulses in optical fibers [3], but also incorporates (linear or nonlinear) gain and loss; it is, thus, a physically relevant variant of a higher-order cubic CGL equation—without the diffusion term. Note that higher-order versions of the CGL equation have only recently started attracting attention [27], while extended second-order CGL models have been extensively studied in various contexts previously [8,14,15]. In particular, we refer to the pioneering work [10], followed by the important contributions [11] and [12], which revealed the existence of the aforementioned low-dimensional dynamical scenarios for second-order quintic CGL models. The results in [10]–[12] were established by numerical and even analytical reductions to suitable finite-dimensional dynamical systems, capturing the long-time dynamics of the original infinite-dimensional one. Notably, the dynamical scenarios revealed were associated with a variety of novel localized structures (known as pulsating solitons).

*dfrantz@phys.uoa.gr

However, a crucial feature of these models as acknowledged, by the authors of [10], is the presence of a higher-order (quintic) nonlinearity. This is a key trait distinguishing that set of works from the present one where only cubic nonlinearity is employed, yet the presence of higher-order effects, most notably third-order dispersion as we see below, plays a catalytic role in the emergence of the relevant phenomenology.

More specifically, we point out that the *third-order cubic* CGL model that we consider herein is essentially different from the *second-order cubic-quintic* model discussed in [10]–[12], not only from a mathematical but also from a physical point of view: indeed, in the context of optics, the model considered in the latter works refers to the propagation of short pulses, in the picosecond regime, in media featuring saturation of the nonlinear refractive index, while the model we consider here is relevant to the propagation of *ultrashort* pulses, in the subpicosecond or femtosecond regime [3]. For this reason, our model includes third-order dispersion and higher-order nonlinear effects, which appear naturally as higher-order corrections of the usual NLS model. In that regard, and if gain and loss are also incorporated, it is important to ask whether, and how, the physically important (on the femtosecond time scale) higher-order effects may be responsible for tracing a path to complex dynamics, as a result of the potential breaking of the homoclinic structure of its unperturbed NLS counterpart.

The main findings of our investigation are the following. First, we show that incorporating gain and loss terms gives rise to the existence of an attractor; a rigorous proof is provided, based on the interpretation of the energy balance equation and properties of the functional (phase) space in which the problem defines an infinite-dimensional flow. The structure of the attractor is then investigated numerically. Given that our model is characterized by six free parameters (which renders a systematic investigation of their role a nontrivial task), we opt to keep four parameters fixed, with values suggested by the physics of ultrashort optical pulses [3], and vary the remaining two. In particular, we vary the coefficients of the third-order dispersion and the higher-order nonlinear dissipation, accounting for the stimulated Raman scattering (SRS) effect (more important reasons for this choice become apparent below). We find that, for a sufficiently small SRS coefficient, variations of the third-order dispersion strength give rise to a transition path from dynamics reminiscent of the PB theorem, including orbital connections between steady states of high multiplicity and convergence to limit cycles, to invariant tori or even chaotic attractors. However, when the SRS effect becomes stronger, the above scenarios are screened by convergence to steady states. It is emphasized that the third-order dispersion is found to be chiefly responsible for a dynamical transition from periodic, to quasiperiodic, and, eventually, to chaotic structures. Therefore, our results show that higher (third)-order dispersion and dissipative (SRS) effects are important mechanisms for the emergence of complex spatiotemporal transitions in CGL models.

Our presentation is organized as follows. In Sec. II, we present the model and discuss the existence of a limit set (attractor). Details on the proof of such a limit set are given in Appendix A. The structure of the attractor is then investigated numerically in Sec. III. We thus reveal the emergence of all

dynamical scenarios and corresponding regimes of complex asymptotic behavior. Finally, Sec. IV summarizes our findings.

II. MOTIVATION AND PRESENTATION OF THE MODEL

Our model is motivated by the higher-order NLS equation

$$i\partial_t u - \frac{s}{2}\partial_x^2 u + |u|^2 u = i\beta\partial_x^3 u + i\mu\partial_x(|u|^2 u) + (\sigma_R + i\nu)u\partial_x(|u|^2), \quad (1)$$

where $u(x,t)$ is a complex field, subscripts denote partial differentiation, β , μ , ν , and σ_R are positive constants, and $s = \pm 1$ denotes the normal (anomalous) group velocity dispersion. Note that Eq. (1) can be viewed as a perturbed NLS equation, with the perturbation (in the case of small values of relevant coefficients) appearing on the right-hand side (see, e.g., Refs. [3] and the discussion below).

Variants of Eq. (1) appear in a variety of physical contexts, where they are derived at higher-order approximations of perturbation theory [the lowest-order nonlinear model is simply the NLS equation on the left-hand side of Eq. (1)]. The most prominent example is probably that of nonlinear optics [3]. In this case, t and x denote the propagation distance and retarded time, respectively, while $u(x,t)$ is the electric-field envelope. While the unperturbed NLS equation is sufficient to describe optical pulse propagation, for ultrashort pulses third-order dispersion and self-steepening (characterized by coefficients β , μ , and ν , respectively) become important and have to be incorporated in the model. Similar situations also occur in other contexts, and thus, corresponding versions of Eq. (2) have been derived and used, e.g., in nonlinear metamaterials [4], but also in water waves at a finite depth [5–7]. Moreover, in the context of optics, and for relatively long propagation distances, higher-order nonlinear dissipative effects, such as the SRS effect, of strength $\sigma_R > 0$, are also important [3].

In addition to the above-mentioned effects, our aim is to investigate the dynamics in the framework of Eq. (1), but also incorporating linear or nonlinear gain and loss. This way, in what follows, we analyze the model

$$i\partial_t u - \frac{s}{2}\partial_x^2 u + |u|^2 u = i\gamma u + i\delta|u|^2 u + i\mu\partial_x(|u|^2 u) + i\beta\partial_x^3 u + (\sigma_R + i\nu)u\partial_x(|u|^2), \quad (2)$$

which includes linear loss ($\gamma < 0$) [linear gain ($\gamma > 0$)]. These effects are physically relevant in nonlinear optics [3,8,14]: indeed, nonlinear gain ($\delta > 0$) [nonlinear loss ($\delta < 0$)] may be used to counterbalance the effects of the linear loss and gain mechanisms and can potentially stabilize optical solitons (see, e.g., Refs. [24] and [25]). As also explained below, here we focus on the case of linear gain, $\gamma > 0$, and nonlinear loss, $\delta < 0$, corresponding to a constant gain distribution and the intensity-dependent two-photon absorption, respectively (see, e.g., Refs. [26]).

Obviously, the presence of gain and loss renders Eq. (2) a higher-order cubic CGL equation (cf. recent studies [27] on such models). Note that in Eq. (2), diffusion is absent: such a linear term would be of the form $iD\partial_x^2 u$ ($D = \text{const}$) and would appear on the right-hand side of Eq. (2) to account for the presence of spectral filtering or linear parabolic gain

($D > 0$) or loss ($D < 0$) [10–12]. Instead, the equation only features linear dispersion through the term proportional to s on the left-hand side of Eq. (2).

The gain and loss effects are pivotal for the dissipative nature of the infinite-dimensional flow that is defined below. This dissipative nature is reflected in the existence of an attractor, capturing its long-time dynamics; nevertheless, as we show below, the structure of the attractor is determined by the remaining higher-order effects.

Here, we focus on the case $s = 1$ and supplement Eq. (2) with periodic boundary conditions for u and its spatial derivatives up to the second order, namely,

$$\begin{aligned} u(x + 2L, t) &= u(x, t) & \text{and} \\ \partial_x^j(x + 2L, t) &= \partial_x^j(x, t), & j = 1, 2, \end{aligned} \quad (3)$$

$\forall (x, t) \in \mathbb{R} \times [0, T]$, for some $T > 0$, where $L > 0$ is given. The initial condition,

$$u(x, 0) = u_0(x), \quad \forall x \in \mathbb{R}, \quad (4)$$

also satisfies the periodicity conditions, (3). Here, we should mention that the periodic boundary conditions that we consider here are also motivated by the context of optics. Recalling that the roles of space and time are interchanged in the latter context, we note that, indeed, in optical cavities (e.g., those for lasers), the period L would account for the (retarded) time it takes light to traverse to the laser cavity once, and thus, the boundaries represent the same point in real space-time (see, e.g., Refs. [28]–[31]). In this context, the dynamics analyzed below are relevant to the dynamical transitions and the observation of chaotic optical waveforms in fiber ring lasers [30].

As shown in Ref. [32], all possible regimes except $\gamma > 0$, $\delta < 0$, are associated with finite-time collapse or decay. Furthermore, a critical value γ^* can be identified in the regime $\gamma < 0$, $\delta > 0$, which separates finite-time collapse from the decay of solutions. On the other hand, for $\gamma > 0$, $\delta < 0$, we prove in Appendix A the existence of a limit set (attractor) $\omega(u_0)$, attracting all bounded orbits initiating from arbitrary, appropriately smooth initial data u_0 (considered elements of a suitable Sobolev space). In the next section, we show numerically that the attractor $\omega(u_0)$ captures the full route from PB-type dynamics to quasiperiodic or chaotic dynamics.

III. NUMERICAL RESULTS

The structure of the limit set $\omega(u_0)$ is investigated by numerical integration via a high-accuracy pseudospectral method. In our simulations, we fix the half-length of Ω to $L = 50$, and the ratio $-\gamma/\delta$ to be of the order of unity, and thus fix $\gamma = 1.5$ and $\delta = -1$. This choice, which stems from the fact that this ratio determines the constant-density steady state (see below), is particularly convenient for illustration purposes. Furthermore, motivated by the fact that, in the context of optics, parameters describing higher-order effects take, typically, small values [3], we fix $\mu = \nu = 0.01$, while third-order dispersion and SRS strengths, $\beta > 0$, $\sigma_R > 0$, are varied in the intervals $[0, 1]$ and $[0, 0.3]$, respectively.

Obviously, the above choice is merely a low-dimensional projection of the full six-dimensional parameter space. Nevertheless, since our scope here is to illustrate the role of

higher-order effects on the emergence of complex dynamics in Eq. (2), we show below that the variations of β and σ_R alone do offer a clear physical picture in that regard. To be more specific, the choice of those particular parameters stems from the following facts. First, third-order dispersion is the sole linear higher-order effect which is important also in the linear regime (as it modifies the linear dispersion relation). Second, the stimulated Raman scattering effect is the first higher-order dissipative effect and, as such, is expected to play a dominant role in the long-time nonlinear dynamics of the system.

Naturally, the nontrivial task (as also highlighted above) of investigating the full parameter space is interesting and relevant in its own right, yet it is beyond the scope of this work.

In our simulations, the limit set $\omega(u_0)$ is visualized by projections of the flow to suitable two-dimensional (2D) or three-dimensional (3D) spaces, defined by $\mathcal{P}_2 = \{(X, Y) \in \mathbb{R}^2\}$ and $\mathcal{P}_3 = \{(X, Y, Z) \in \mathbb{R}^3\}$. Here, $X(t) = |u(x_1, t)|^2$, $Y(t) = |u(x_2, t)|^2$, $Z(t) = |u(x_3, t)|^2$ for arbitrary spatial coordinates $x_1, x_2, x_3 \in \Omega$.

A. Steady-state and orbital connections regime

First, we use continuous wave (cw) initial data,

$$u_0(x) = \epsilon \exp\left(-i \frac{K\pi x}{L}\right) \equiv \epsilon \phi_K,$$

of amplitude $\epsilon > 0$ and wave number $K > 0$, which is an element of the 1D linear subspace

$$\mathcal{V}_K = \{u \in L^2(\Omega) : u = \epsilon \phi_K(x), \epsilon > 0\}$$

of $L^2(\Omega)$. Here we should note that there exists a cw state which is an exact solution of Eq. (2); this solution is generically subject to modulational instability (MI) [33] (so-called Benjamin-Feir instability in the context of deep water waves [34]). The exact cw solution, as well as the relevant MI analysis, is presented in Appendix B. However, this analysis is not capable of providing any insights into the long-time dynamics of the solutions. Indeed, although it can be used as a means to understand the destabilization of the cw steady state, it does not offer any information regarding the long-time behavior and the states the system passes through. As we show below, the intricate dynamics that emerge cannot be fully understood in the framework of the MI picture.

Using the above cw initial data and varying $\sigma_R > 0$, we find that $\omega(u_0)$ is an equilibrium state. Specifically, there exists a critical wave number K_{\max} such that, for $K < K_{\max}$, $\omega(u_0) = \phi_b$, i.e., a steady state of constant density $|\phi_b|^2 = -\frac{\gamma}{\delta}$, and for $K \geq K_{\max}$, $\omega(u_0) = \Phi_p$, i.e., a steady state of spatially periodic density. We find that K_{\max} decreases as σ_R increases: if $\sigma_R = 0, 0.1, 0.2$, and 0.3 , and $\beta = 0.02$, then $K_{\max} = 16, 13, 10$, and 5 , respectively.

The dynamical scenario $\omega(u_0) = \{\phi_b\}$ for $\beta = 0.02$, $\sigma_R = 0.3$, and $K = 4$ is illustrated in Fig. 1. The projection of the cw equilibrium ϕ_b to the 2D space \mathcal{P}_2 is the fixed point $\mathbf{A} = (|\phi_b|^2, |\phi_b|^2) = (-\frac{\gamma}{\delta}, -\frac{\gamma}{\delta}) = (1.5, 1.5)$. The right panel in Fig. 1 illustrates the convergence of the projected linear orbits to \mathbf{A} , associated with the choice of spatial coordinates $x_1 = 5$, $x_2 = 10$. The dashed blue (solid red) line is the projection of the flow for the cw with $\epsilon = 3$ ($\epsilon = 0.01$); the arrows

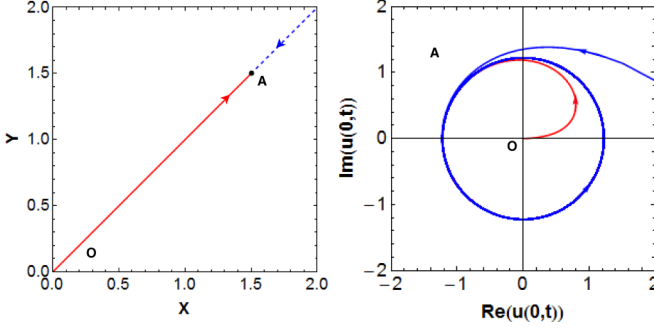


FIG. 1. The scenario $\omega(u_0) = \{\phi_b\}$. Left: Convergence to fixed point **A**. Right: Fixed point **A** as a limit circle of radius $\sqrt{-\gamma/\delta}$.

indicate the direction of the 2D projection of the flow. The cw steady state ϕ_b is an element of \mathcal{V}_K and differs from the initial condition only in amplitude. Hence, \mathcal{V}_K defines a stable linear subspace for **A**. The right panel in Fig. 1 shows the steady-state ϕ_b as a limit circle **A** of radius $\sqrt{-\frac{\gamma}{\delta}} = \sqrt{1.5}$, in the 2D space $\text{Re}(u(0,t)), \text{Im}(u(0,t))$. The limit circle corresponds to the rotating linear oscillations of the real and imaginary parts of the solution u . Effectively in this case, the solution preserves its plane-wave form but its amplitude, say $h(t)$, satisfies a Bernoulli equation. This can be seen as follows: we substitute $u(x,t) = W(t)e^{iKx}$ in Eq. (2) and obtain the following equation for the time-dependent amplitude $W(t)$ (as usual, overdots denote time derivatives):

$$i\dot{W} - \frac{1}{2}K^2W + |W|^2W = i\gamma W + i\delta|W|^2W + \beta K^3W - \mu KW. \quad (5)$$

Then, taking $W(t) = h(t)\exp[i(K^2/2 - \beta K^3 + \mu K)t]$, we obtain from Eq. (5) the Bernoulli equation:

$$\dot{h} = \gamma h + \delta h^3.$$

Thus, for $h(0) = \epsilon$,

$$\lim_{t \rightarrow \infty} h^2(t) = -\frac{\gamma}{\delta} \equiv |\phi_b|^2.$$

Next, consider the scenario $\omega(u_0) = \{\Phi_p\}$, for $\beta = 0.02\sigma_R = 0.3$, and $K = 5$, illustrated in Fig. 2. The upper panel shows density snapshots for a cw initial condition with $\epsilon = 0.01$. The solution has reached the cw steady state ϕ_b exponentially rapidly, but at $t \approx 500$ the instability of the state ϕ_b emerges. Although transient oscillations of increasing amplitude occur (cf. snapshot at $t = 683$) due to the linear gain $\gamma > 0$, the nonlinear loss $\delta < 0$ prevents collapse of the solution. After $t \approx 685$, we observe convergence to the new steady state Φ_p (reached at $t \approx 700$), whose profile remains unchanged till the end of integration ($t = 3000$). The orbital connection, via the transient dynamics, between steady state ϕ_b and steady state Φ_p is illustrated in the projections of the flow on the spaces \mathcal{P}_2 and \mathcal{P}_3 ; cf. lower-left and lower-right panels in Fig. 2, respectively, for $x_1 = 0$ and $x_2 = 4.5$. In two dimensions, **B** $\approx (1.5, 0.15)$ is the new fixed point, while in three dimensions, **A** $= (1.5, 1.5, 1.5)$ and **B** $\approx (1.5, 0.15, 1.16)$. The infinite-dimensional orbital connection,

$$\{0\} \text{ (unstable)} \xrightarrow{\mathcal{O}_1} \{\phi_b\} \text{ (unstable)} \xrightarrow{\mathcal{O}_2} \{\Phi_p\} = \omega(u_0),$$

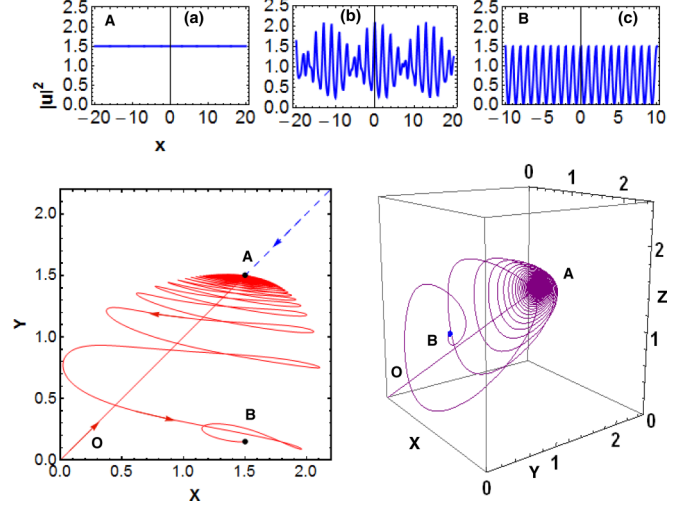


FIG. 2. The scenario $\omega(u_0) = \{\Phi_p\}$. Upper panels: Density snapshots at times (a) $t \approx 500$, (b) $t \approx 683$, and (c) $t \approx 700$. Lower panels: Orbital connections $\mathbf{O} \rightarrow \mathbf{A} \rightarrow \mathbf{B}$ in 2D (left) and 3D (right) spaces.

where \mathcal{O}_1 and \mathcal{O}_2 denote the orbits connecting the steady states, is projected to the 2D and 3D connections:

$$\mathbf{O} \text{ (unstable)} \xrightarrow{\mathcal{O}'_1} \{\mathbf{A}\} \text{ (unstable)} \xrightarrow{\mathcal{O}'_2} \{\mathbf{B}\}.$$

The projected orbits highlight the spiraling of the stable manifold of the limit point **B** around the unstable linear subspace of $\mathbf{O} = (0, 0, 0)$ connecting \mathbf{O} and **A**. The connection was found to be stable with respect to variations of ϵ ; cf. dashed blue (solid red) linear converging orbit in the lower-left panel, corresponding to a cw initial condition of amplitude $\epsilon = 2$ ($\epsilon = 0.01$).

B. Space-time periodic (limit-cycle) regime

Upon increasing β , for $\sigma_R = 0.01$, we observe the birth of yet another feature, namely, traveling space-time oscillations. The upper panel in Fig. 3 shows density snapshots for a cw initial condition of $K = 5$, $\epsilon = 0.01$, and $\beta = 0.55$. Now, instability of the steady state ϕ_b leads to the birth of a stable, traveling space-time periodic solution, whose profile is shown for $t = 180$ (arrow indicates the propagation direction). The projections for $x_1 = 0$, $x_2 = 5$, and $x_3 = 10$ on \mathcal{P}_2 (lower-left panel) and \mathcal{P}_3 (lower-right panel) illustrate the periodic solution as a limit cycle **L**, i.e., a periodic orbit. The solid blue (dashed red) linear orbit shown in the lower-left panel corresponds to the cw initial conditions of $K = 5$ and $\epsilon = 3$ ($\epsilon = 0.01$), highlighting the stability (i.e., attracting nature) of the limit cycle with respect to ϵ . Specifically, for fixed $\sigma_R = 0.01$ and $K > 4$, there exists an interval $I_{\beta,K} = [\beta_{\min}(K), \beta_{\max}(K)]$ such that for some $\beta \in I_{\beta,K}$, the initial condition may converge to a space-time periodic solution; e.g., for $K = 5$, $I_{\beta,5} \approx [0.5, 0.57]$, while for $K = 20$, $I_{\beta,20} \approx [0.7, 1.2]$. On the other hand, when $\beta \notin I_{\beta,K}$, the initial condition converges to a steady state. Evidently, the structure of the limit set $\omega(u_0)$ for Eq. (2), consisting either of distinct equilibria and orbits connecting them or of a limit cycle, is reminiscent of scenarios associated with PB dynamics.

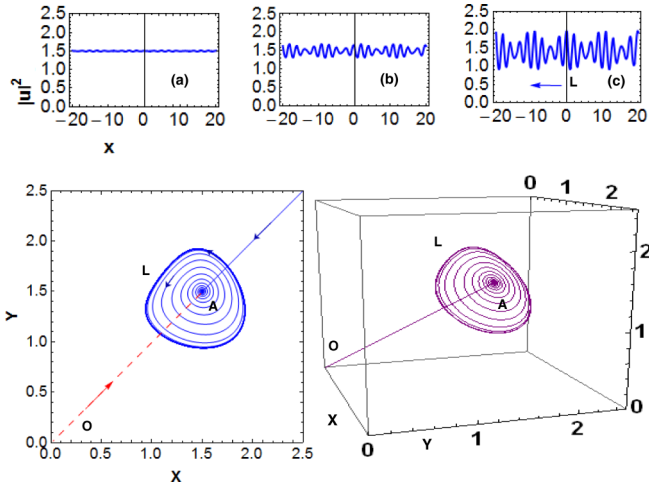


FIG. 3. Dynamics scenario $\omega(u_0) = \mathbf{L}$, i.e., a space-time periodic traveling wave. Upper panels: Density snapshots at times (a) $t \approx 135$, (b) $t \approx 150$, and (c) $t \approx 180$. Lower panels: Convergence $\mathbf{O} \rightarrow \mathbf{A} \rightarrow \mathbf{L}$, the limit cycle in 2D (left) and 3D (right) spaces.

It is important to remark that third-order dispersion plays a critical role in this scenario of $\omega(u_0) = \mathbf{L}$, as it can be *chiefly* responsible for the emergence of a limit cycle. Indeed, Fig. 4 shows the dynamics for a cw initial condition of $K = 15$ and amplitudes as in Fig. 3, but for $\beta = 0.02$ and $\sigma_R = \mu = \nu = 0$. Furthermore, the third-order dispersion alone can also give rise to even more complex behavior (see below).

C. Quasiperiodic and chaotic regime

The interval $I_{\beta,K}$ may be partitioned to subintervals where quasiperiodic or even chaotic behavior emerges. Figure 5 shows the 3D projection of the flow on \mathcal{P}_3 , for $x_1 = 5, x_2 = 10$,

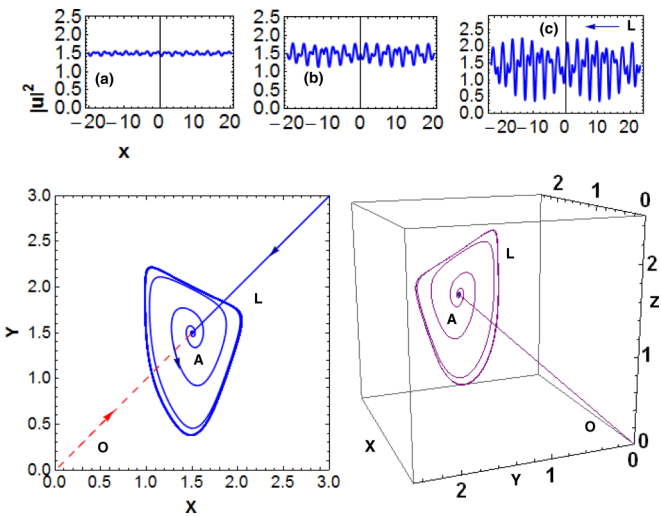


FIG. 4. Dynamics scenario $\omega(u_0) = \mathbf{L}$, in the presence of third-order dispersion only, namely, for $\beta = 0.02$ and $\mu = \nu = \sigma_R = 0$. Upper panel: Density snapshots at times (a) $t \approx 400$, (b) $t \approx 420$, and (c) $t \approx 450$, for a single-cw initial condition of $K = 15$, $\epsilon = 0.01$, and $\beta = 0.02$. Lower panels: Convergence $\mathbf{O} \rightarrow \mathbf{A} \rightarrow \mathbf{L}$, i.e., the stable limit cycle, in the 2D (left) and 3D (right) spaces.

$x_3 = 15, t \in [0, 350], \beta = 0.52$, and $\sigma_R = \mu = \nu = 0.01$, for cw conditions of $\epsilon = 0.01$ and $K = 5$. We observe the birth of quasiperiodic orbits from the instability of the steady state ϕ_b and the transition to chaotic behavior manifested by their trapping to a chaotic attractor \mathbf{S} .

The upper-left panel in Fig. 6 shows part of a chaotic orbit in \mathbf{S} for $t \in [180, 200]$ and $\beta = 0.5 \approx \beta_{\min}(5)$. The first two snapshots in the lower panel show profiles of the solution corresponding to points $\mathbf{P1}$ and $\mathbf{P2}$, for $t = 150$ and $t = 165$. The “windings” of the chaotic orbits are evident in the upper-left panel in Fig. 6 and similarly, also, in the lower-right panel in Fig. 5. The chaotic behavior manifests itself in the time-fluctuating amplitude, the changes in the waveform’s spatial periodicity, and the propagation direction of the chaotic traveling wave.

The interval $I_{\beta,K} = [\beta_{\min}(K), \beta_{\max}(K)]$ can be partitioned into the following subintervals: a chaotic, $I_{\beta,K,c} = [\beta_{\min}(K), \beta_{\text{ch}}(K)]$, a quasiperiodic, $I_{\beta,K,q} = (\beta_{\text{ch}}(K), \beta_{\text{lc}}(K))$, and a limit-cycle, $I_{\beta,K,lc} = [\beta_{\text{lc}}(K), \beta_{\max}(K)]$, subinterval. Let $\beta_{\min}(K)$ be the critical value for the onset of quasiperiodic behavior and the transition to the chaotic regime. Then, as $\beta \rightarrow \beta_{\text{ch}}(K)$, the chaotic features are less evident and emerge at later times. Chaotic orbits still exist for $\beta = \beta_{\text{ch}}(K)$. For $\beta > \beta_{\text{ch}}(K)$, solutions remain quasiperiodic, and the orbit is trapped within an invariant torus-like set \mathbf{Q} . For $K = 5$, we find that $\beta_{\text{ch}}(5) \approx 0.53$. The projection on \mathcal{P}_3 of \mathbf{Q} for $\beta = 0.54 > \beta_{\text{ch}}(5)$ is shown in the upper-right panel in Fig. 6. The orbit is plotted for $t \in [1800, 2000]$, and the profile of a quasiperiodic solution within \mathbf{Q} at $t = 1900$ is shown in the third snapshot in the lower panel. The set \mathbf{Q} persists as long as $\beta < \beta_{\text{lc}}(K)$. When $\beta_{\text{lc}}(K) \leq \beta \leq \beta_{\max}(K)$, set \mathbf{Q} is replaced by a limit cycle. For $K = 5$, we find the following subintervals of $I_{\beta,5} \approx [0.5, 0.57]$: the chaotic, $I_{\beta,5,c} \approx [0.5, 0.53]$, the quasiperiodic,

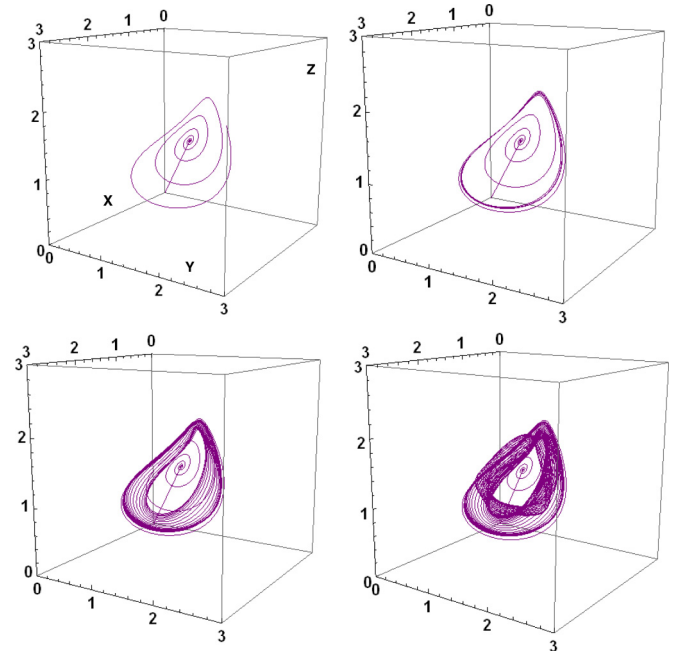


FIG. 5. Birth of a chaotic attractor $\omega(u_0) = \mathbf{S}$. Transition from the instability of the cw steady state \mathbf{A} , to quasiperiodic behavior, and then to chaotic behavior for $t \in [0, 330]$.

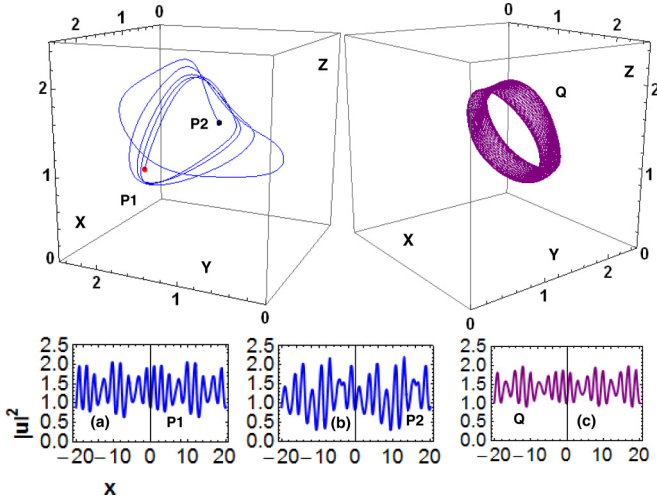


FIG. 6. Upper panels: A chaotic path in \mathcal{S} for $t \in [180,200]$ (left) and projection in 3D space \mathcal{P}_3 of the invariant torus-like set \mathcal{Q} for $t \in [1800,2000]$ (right). Lower panels: Chaotic waveforms, corresponding to point $\mathbf{P1}$ at time $t \approx 150$ (left) and point $\mathbf{P2}$ at time $t \approx 165$ (middle), and a quasiperiodic solution in \mathcal{Q} at time $t \approx 1900$ (right).

$I_{\beta,5,q} \approx (0.53,0.55)$, and the limit-cycle, $I_{\beta,5,lc} \approx [0.55,0.57]$, subintervals. For $K = 5$, the above subintervals were detected with accuracy 10^{-3} : for $\beta = 0.549$, set \mathcal{Q} persists, while for $\beta = 0.55$, the initial state is trapped in the limit cycle.

D. Numerical bifurcation diagrams

The richness of the dynamics can be summarized in a bifurcation diagnostic (“diagnostic I”), namely, the $\beta - \|u\|_\infty$ bifurcation diagram, shown in the upper panel in Fig. 7. The bifurcation curve (solid blue line) illustrates the variations of the $\|u\|_\infty$ norm of the solutions, defined as

$$\|u\|_\infty = \max_{(x,t) \in D} |u(x,t)|, \quad D = [-L, L] \times [0, T_{\max}],$$

where T_{\max} denotes the end of the interval of numerical integration $[0, T_{\max}]$; the third-order dispersion coefficient is $\beta \in [0,1]$, while the rest of the parameters are fixed to the values $\sigma_R = \mu = \nu = 0.01$, and for the cw initial conditions we use $\epsilon = 0.01$ and $K = 5$. The system was integrated until $T_{\max} = 3000$. The branches AB and FG correspond to the intervals $\beta \in [0,0.18]$ and $\beta \in (0.57, 1]$, respectively, and are associated with the dynamical scenario $\omega(u_0) = \{\phi_b\}$, i.e., convergence to the steady state of constant density, $|\phi_b|^2 = -\frac{\nu}{\delta}$. The intersection of the bifurcation curve with the auxiliary “separatrix” B, at $\beta \approx 0.18$, designates the transition to the equilibrium metastability region BC (yellow shaded area), in the interval $\beta \in [0.18,0.5]$. Fluctuations of the bifurcation curve are associated with metastable dynamical scenarios between distinct states. One such scenario may refer to the orbital connections between steady states mentioned above; another one may correspond to a transition from unstable periodic orbits to chaotic oscillations and an eventual convergence to steady state. These scenarios are followed by drastically different transient dynamics characterizing these connections.

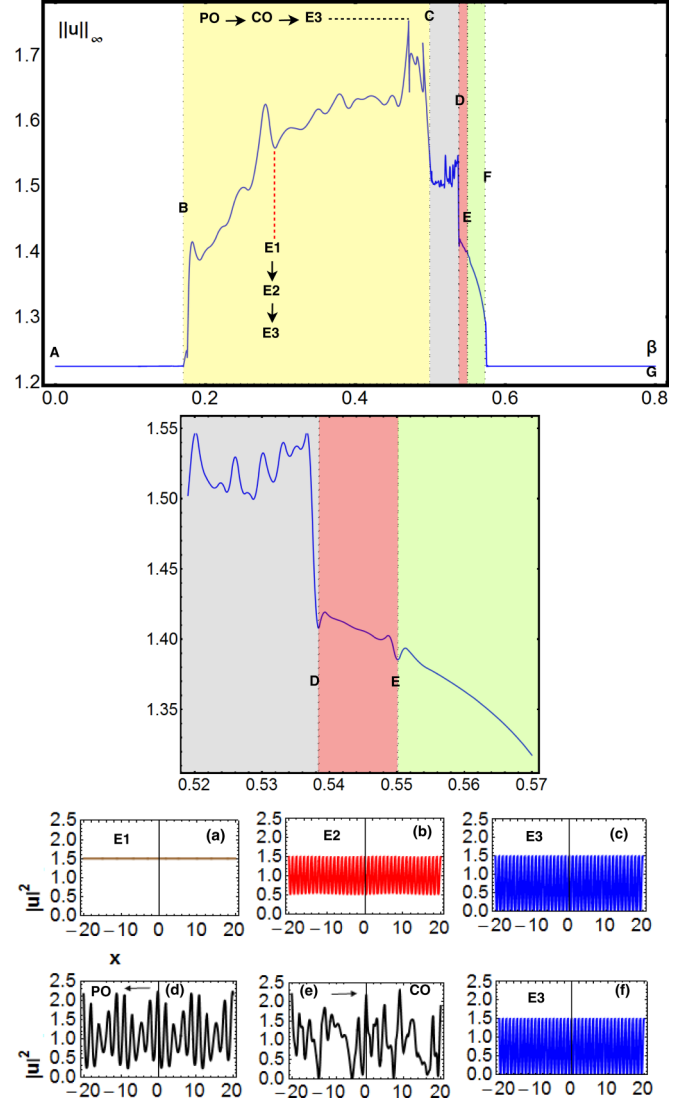


FIG. 7. From top to bottom. First row: $\beta - \|u\|_\infty$ bifurcation diagram (Diagnostic I) for fixed $\sigma_R = \mu = \nu = 0.01$ and the cw initial conditions of $\epsilon = 0.01$ and $K = 5$. Second row: Magnification of the quasiperiodic region DE shown in the preceding panel. Third row: Profiles of the distinct steady states involved in the orbital connection $\mathbf{E1} \rightarrow \mathbf{E2} \rightarrow \mathbf{E3}$ occurring at $\beta = 0.3$ in the metastable region BC. The system is at rest in steady state $\mathbf{E1}$ for $5 \lesssim t \lesssim 35$, in $\mathbf{E2}$ for $60 \lesssim t \lesssim 68$, and in $\mathbf{E3}$ for $100 \lesssim t \lesssim 3000$, which is the end of integration. Fourth row: Transition from an unstable periodic orbit (\mathbf{PO}) to chaotic oscillations (\mathbf{CH}) which are eventually damped to steady state $\mathbf{E3}$. The unstable periodic orbit (\mathbf{PO}) survives for $62 \lesssim t \lesssim 105$, and the chaotic orbit for $120 \lesssim t \lesssim 203$. The system is at rest in steady state $\mathbf{E3}$ for $217 \lesssim t \lesssim 3000$, which is the end of integration.

As the first example, we note the metastable transition— at $\beta = 0.3$ (vertical dashed red line)—between three distinct steady states, $\mathbf{E1} \rightarrow \mathbf{E2} \rightarrow \mathbf{E3}$ (with $\mathbf{E1}$ labeling the steady state of constant density, $|\phi_b|^2 = -\frac{\nu}{\delta}$). The third-row in Fig. 7 shows the density profiles of these steady states. The second example refers to the transition from an unstable periodic orbit, \mathbf{PO} (which emerges from the instability of the steady state ϕ_b), to chaotic oscillations, \mathbf{CO} , and the convergence to

the final steady-state, **E3**; this transition occurs for $\beta = 0.47$ (horizontal dashed black line). Density profiles during this transition are shown in the fourth row in Fig. 7. For the first example, the ultimate state **E3** is reached at $t \approx 103$, and the solution remains unchanged until the end of integration, while for the second example, the ultimate state **E3** is reached at $t \approx 217$.

The intersection of the bifurcation curve with the second auxiliary separatrix C, with an almost-vertical slope, is associated with the transition to the chaotic region CD (gray shaded area in Fig. 7), corresponding to the interval $I_{\beta,5,c} \approx [0.5, 0.53]$. The sudden jump of the bifurcation curve (with an infinite slope) at the intersection with separatrix D designates the entrance into the quasiperiodic regime DE (pale-red shaded area), associated with the interval $I_{\beta,5,q} \approx (0.53, 0.55)$. This region is magnified in the second row in Fig. 7. On the other hand, the next steep jump, at the intersection with separatrix E (also magnified in the second row in Fig. 7), depicts the entrance to the space-time periodic regime EF (pale-green shaded area), associated with the limit-cycle interval $I_{\beta,5,l,c} \approx [0.55, 0.57]$. The limit-cycle branch bifurcates from the intersection with separatrix F, beyond which the branch of the constant-density steady state FG is traced.

Another bifurcation diagnostic (Diagnostic II) that we use herein is the one associated with the variation of the quantity

$$\|u(T_{\max})\|_{\alpha}^2 = \frac{1}{2L} \int_{-L}^L |u(x, T_{\max})|^2 dx$$

with respect to β . For sufficiently large T_{\max} , $\|u(T_{\max})\|_{\alpha}^2$ can be thought of as the superior limit of Eq. (A2). The drawback in the above diagnostic is that the transient dynamics are hidden (for sufficiently large T_{\max}); more generally, the result hinges strongly on the selection of T_{\max} , but not necessarily strongly on the evolution for earlier times or mirroring that for later times. Nevertheless, for sufficiently large T_{\max} , it can be particularly useful in detecting convergence to different steady states, e.g., $\omega(u_0) = \{\phi_b\}$ or $\omega(u_0) = \{\Phi_p\}$, via metastability. Furthermore, it is also able to detect regimes of more complex behavior, similarly to the $\|u\|_{\infty}$ diagnostic. Figure 8 shows the $\beta - \|u(T_{\max})\|_{\alpha}^2$ bifurcation curve (solid red line) for $T_{\max} = 3000$; the rest of the parameters are as in Fig. 7. The four shaded regions correspond to the same distinct dynamical regimes that were detected in the $\beta - \|u\|_{\infty}$ bifurcation diagram in Fig. 7. The horizontal straight lines

$$\|u(T_{\max})\|_{\alpha}^2 = 1.5 = -\frac{\gamma}{\delta}$$

in regions AB and FG show that, in these regimes of β , solutions converge to the steady state ϕ_b . The intersection of the bifurcation curve with the auxiliary ‘‘separatrix’’ B, at $\beta \approx 0.18$, still designates the transition to the equilibrium metastability region BC. However, the new straight horizontal line $\|u(T_{\max})\|_{\alpha}^2 = 0.68$ clearly shows that, after the transient metastability dynamics, the solution favors a particular steady state of convergence, namely, **E3** for these parameters.

It is now useful to compare Diagnostics I and II. First, we note that the comparison between the two in the metastability regime BC reveals that far from equilibrium transient dynamics are identified only by the fluctuations in the $\beta - \|u\|_{\infty}$ curve (Diagnostic I)—and *not* those in the $\beta - \|u(T_{\max})\|_{\alpha}^2$ curve

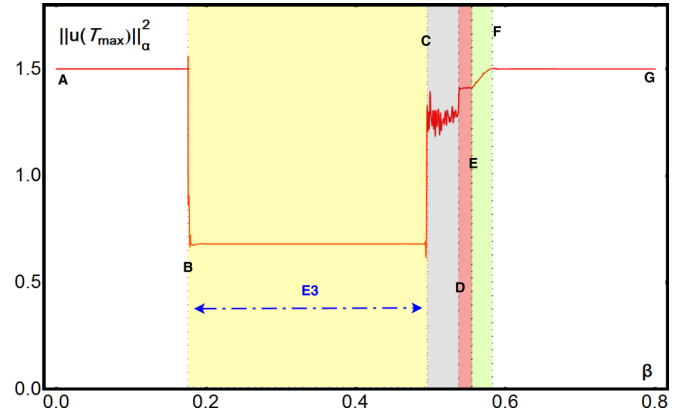


FIG. 8. $\beta - \|u(T_{\max})\|_{\alpha}^2$ bifurcation diagram (Diagnostic II) for fixed $\sigma_R = \mu = \nu = 0.01$ and the cw initial conditions of $\epsilon = 0.01$ and $K = 5$.

(Diagnostic II). These fluctuations can be understood by the fact that $\|u\|_{\infty}$ may be reached at a certain instant, $t_0 \in [0, T_{\max}]$, and also by noting that, in general, $\|u\|_{\infty} \neq \max_{-L \leq x \leq L} |\Phi(x)|$ [i.e., the $\|u\|_{\infty}$ norm of a steady state $\Phi(x)$]. Diagnostic II, on the other hand, reveals that in the metastability regime BC, the dynamics favors a distinct steady state (as mentioned above)—a fact that cannot be captured by Diagnostic I. As far as the other regimes are concerned, Diagnostic II can also capture the transition to the chaotic regime CD, indicated by the intersection of the bifurcation curve with the auxiliary separatrix C, as well as by its large rapid fluctuations within region CD. The sudden jump of the bifurcation curve at the intersection with separatrix D designates the entrance into the quasiperiodic regime, portrayed by the small, almost-horizontal branch of quasiperiodic solutions within region DE. Note that the transition to the quasiperiodic regime is much more apparent in Diagnostic II than in Diagnostic I. The intersection of the bifurcation curve with separatrix E (at a point where the curve has a local minimum in region DF) is again associated with the entrance to the space-time periodic regime EF (corresponding to the branch of space-time periodic solutions). This branch bifurcates from the straight line FG (pertinent to constant-density steady states) at its intersection with separatrix F.

It is important, at this point, to make some additional remarks. First, the interval $I_{\beta,K}$, corresponding to region CF in the bifurcation diagrams, was found to be unstable under variations of $\sigma_R > 0$. Corresponding (in)stability regimes are illustrated in the top panel in Fig. 9, where a Diagnostic II-type diagram is shown, namely, the bifurcation curve $\sigma_R - \|u(T_{\max})\|_{\alpha}^2$ (solid red line). This diagram is plotted for fixed $T_{\max} = 3000$ and $\beta = 0.52$ (recall that, in the previous case, for fixed $\sigma_R = 0.01$, it was found that $\beta = 0.52 \in I_{\beta,5,c} \approx [0.5, 0.53]$, i.e., in the chaotic regime); the rest of the parameters are as in Fig. 7. It is shown that for relatively small values of the SRS coefficient, namely, for $\sigma_R < 0.03$ (cf. the gray shaded area, labeled SR), chaotic behavior persists. On the other hand, above this threshold, i.e., for $\sigma_R > 0.03$, chaotic structures are destroyed, and the system enters into the metastability regime (labeled RW in the diagram). The ultimate steady state is **E3** for these parameters. Note that the

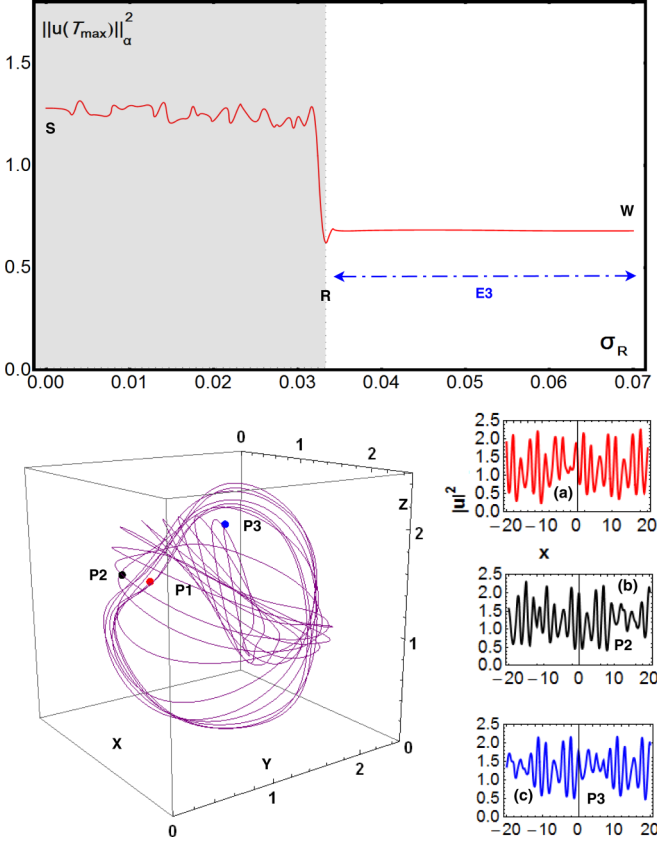


FIG. 9. Upper panel: $\sigma_R - \|u(T_{\max})\|_\alpha^2$ bifurcation diagram (Diagnostic II) for fixed $\beta = 0.52$, $\mu = \nu = 0.01$, and the cw initial conditions of $\epsilon = 0.01$ and $K = 5$. Lower-left panel: A chaotic path for $t \in [600, 650]$, when $\beta = 0.53$, $\sigma_R = \mu = \nu = 0$, and the initial conditions are as in the upper panel. Lower-right panel: Chaotic waveforms corresponding to points **P1** at $t \approx 600$ (top), **P2** at $t \approx 625$ (middle), and **P3** at $t \approx 650$ (bottom).

instability of quasiperiodic and space-time periodic regimes under the influence of small increments in σ_R , occurs in a very similar manner and can be plotted in similar bifurcation diagrams (results not shown here).

Second, the interval $I_{\beta, K}$ persists even in the absence of the rest of the higher-order effects, i.e., for $\sigma_R = \mu = \nu = 0$. This highlights the fact that the third-order dispersion plays a dominant role in the emergence of complex dynamics. An example of the chaotic behavior, for $\beta = 0.53$ and $\mu = \nu = \sigma_R = 0$, is shown in the lower panel in Fig. 9. In particular, the lower-left plot shows part of a chaotic orbit for $t \in [600, 650]$ of the 3D projection of the flow on \mathcal{P}_3 , for $x_1 = 5$, $x_2 = 10$, and $x_3 = 15$. Furthermore, the three snapshots in the lower-right plots show profiles of the solution corresponding to points **P1**, **P2**, and **P3** of the chaotic path shown on the left, for $t = 600$, $t = 625$, and $t = 650$, respectively.

IV. CONCLUSIONS

In conclusion, we have studied a physically important and broadly relevant higher-order Ginzburg-Landau equation, with zero diffusion. The considered model is motivated by a higher-order nonlinear Schrödinger equation, which finds

applications in a variety of contexts, ranging from nonlinear fiber optics to deep water waves; the model also incorporates linear loss and nonlinear gain, while it is supplemented with periodic boundary conditions which are relevant to optical cavities settings such as those employed, e.g., in ring lasers.

Our analysis reveals that the infinite-dimensional dynamics of this model can be reduced to a sequence of low-dimensional dynamical scenarios (fixed points, periodic and quasiperiodic, as well as chaotic, orbits) that can be suitably revealed in reduced (2D and 3D) phase-space representations. Such a dynamical picture is shared by various nonintegrable perturbations of Hamiltonian partial differential equations (such as the NLS and Sine-Gordon equations), as these perturbations may break the homoclinic structure of their integrable counterparts. However, the path to all the above dynamical scenarios can be traced in drastically different ways and to essentially distinct roots, even if the systems have similar origins for their dissipative nature manifested by the existence of an attractor, e.g., due to the presence of gain or loss, as in the case of CGL models.

In particular, in our higher-order CGL model, keeping gain and loss—as well as other coefficients of the higher-order effects—fixed, we have shown that the competition between third-order dispersion and the SRS effect (in the presence of nonlinearity, dispersion, and gain or loss) can trace a path from Poincaré-Bendixson-type behavior to quasiperiodic or chaotic dynamics. These dynamical transitions are also reminiscent of those observed in fiber ring lasers or in the path towards optical turbulence phenomena [30,35]. A conspicuous finding is that third-order dispersion chiefly appears to play a critical role in controlling the transition from periodic to quasiperiodic, and eventually to chaotic, behavior, even in the absence of the rest of the higher-order effects.

Our results highlight that higher-order effects may play a primary role in the birth of spatiotemporal transitions in mixed gain-loss systems, suggesting further investigations. First, in the framework of the model considered here, it would be particularly interesting to investigate more broadly the full six-parameter space, rather than its low-dimensional projection considered herein. Second, another interesting direction would be the identification of a low-dimensional attractor, its dimension, and its dependence on the spatial length [21], as well as the construction of appropriate finite-dimensional reduced systems able to capture the effective low-dimensional dynamics [36]. Finally, it would be interesting to investigate the role of higher-order effects in other autonomous systems with gain and loss.

ACKNOWLEDGMENTS

D.J.F., N.I.K., and P.G.K. gratefully acknowledge the support of QNRF Grant No. NPRP8-764-1-160.

APPENDIX A: EXISTENCE OF A LIMIT SET (ATTRACTOR)

In this Appendix, we define an extended dynamical system associated with the initial boundary value problem, (2)–(4). In particular, we briefly sketch the proof of the existence of a limit-set attractor, capturing all bounded orbits of this

dynamical system, which originates from sufficiently smooth initial data, (4).

The starting point of our proof is the power balance equation [37],

$$\frac{d}{dt} \int_{-L}^L |u|^2 dx = 2\gamma \int_{-L}^L |u|^2 dx + 2\delta \int_{-L}^L |u|^4 dx, \quad (\text{A1})$$

satisfied by any local solution $u \in C([0, T], H_{\text{per}}^k(\Omega))$, which originates from sufficiently smooth initial data $u_0 \in H_{\text{per}}^k(\Omega)$, for fixed $k \geq 3$. Here, $H_{\text{per}}^k(\Omega)$ denotes the Sobolev spaces of periodic functions H_{per}^k [38], in the fundamental interval $\Omega = [-L, L]$:

$$H_{\text{per}}^k(\Omega) = \{u : \Omega \rightarrow \mathbb{C}, u \text{ and } \partial_x^j u \in L^2(\Omega), j = 1, \dots, k; \\ u \text{ and } \partial_x^j u \text{ for } j = 1, \dots, k-1 \text{ are } 2L\text{-periodic}\}.$$

Analysis of (A1) results in the asymptotic estimate,

$$\limsup_{t \rightarrow \infty} \frac{1}{2L} \int_{-L}^L |u(x, t)|^2 dx \leq -\frac{\gamma}{\delta}; \quad (\text{A2})$$

hence local in time solutions $u \in C([0, T], H_{\text{per}}^k(\Omega))$ are uniformly bounded in $L^2(\Omega)$. This allows for the definition of the extended dynamical system

$$\varphi(t, u_0) : H_{\text{per}}^k(\Omega) \rightarrow L^2(\Omega), \quad \varphi(t, u_0) = u,$$

whose orbits are bounded $\forall t \geq 0$. Moreover, from the above asymptotic estimate, we derive that if $L^2(\Omega)$ is endowed with the equivalent averaged norm,

$$\|u\|_{\alpha}^2 = \frac{1}{2L} \int_{-L}^L |u|^2 dx,$$

then its ball

$$\mathcal{B}_{\alpha}(0, \rho) = \left\{ u \in L^2(\Omega) : \|u\|_{\alpha}^2 \leq \rho^2, \rho^2 > -\frac{\gamma}{\delta} \right\}$$

attracts all bounded sets $\mathcal{B} \in H_{\text{per}}^k(\Omega)$. That is, there exists $T^* > 0$, such that $\varphi(t, \mathcal{B}) \subset \mathcal{B}_{\alpha}$, for all $t \geq T^*$. Thus, we may define for any bounded set $\mathcal{B} \in H_{\text{per}}^k(\Omega)$, $k \geq 3$, its ω -limit set in $L^2(\Omega)$:

$$\omega(\mathcal{B}) = \bigcap_{s \geq 0} \overline{\bigcup_{t \geq s} \varphi(t, \mathcal{B})}.$$

The closures are taken with respect to the weak topology of $L^2(\Omega)$. Then the standard (embedding) properties of Sobolev spaces imply that the attractor $\omega(\mathcal{B})$ is at least weakly compact in $L^2(\Omega)$ or relatively compact in the dual space $H_{\text{per}}^{-1}(\Omega)$. For any initial condition (4), $u_0 \in \mathcal{B}$, we denote its limit set $\omega(u_0) \subset \omega(\mathcal{B})$.

APPENDIX B: MODULATIONAL INSTABILITY

In this Appendix we provide the MI analysis of the cw state,

$$u = u(t) = A e^{i\theta(x, t)}, \quad \theta(x, t) = k_0 x - \omega_0 t \quad (\text{B1})$$

(where A is a real constant), which is an exact analytical solution of Eq. (2) (for an MI analysis of the cw solution of Eq. (1), cf. Ref. [39]). This solution exists when the following dispersion relation holds:

$$\omega_0 = \beta k_0^3 - k_0^2/2 - \mu A^2 k_0 + i(\gamma + \delta A^2) - A^2,$$

while $A^2 = -\gamma/\delta$, to suppress any exponential growth. This amplitude value is consistent with the equilibria (steady states) of the system.

Now consider a small perturbation to this cw solution,

$$u(x, t) = [A + u_1(x, t)] e^{i\theta(x, t)},$$

inserted into Eq. (2). Linearizing the system with respect to u_1 we obtain

$$i(u_{1t} - k_0 u_{1x}) - \frac{1}{2} u_{1xx} + A^2(u_1 + u_1^*) = i\delta A^2(u_1 + u_1^*) \\ + i\beta(3k_0^2 u_{1x} - 3ik_0 u_{1xx} - u_{1xxx}) \\ - i\mu A^2(ik_0 u_1 + ik_0 u_1^* + 2u_{1x} + u_{1x}^*) \\ - i(\nu - i\sigma_R) A^2(u_{1x} + u_{1x}^*),$$

where asterisks denote complex conjugates. Solutions of the above equations are sought in the form

$$u_1(x, t) = c_1 e^{i(kx - \omega t)} + c_2 e^{-i(kx - \omega t)},$$

where $c_{1,2}$ are real constants, while k and ω are the wave number and frequency of the perturbations. In this way, we obtain the dispersion relation,

$$\delta^2 \omega^2 + p_1(k)\omega + p_2(k) = 0 \quad (\text{B2})$$

where

$$p_1(k) = -2\beta k^3 + 2[-3\beta k_0^2 + k_0 + A^2(2\mu + \nu - i\sigma_R)]k, \\ p_2(k) = \beta^2 k^6 \\ + [-3\beta^2 k_0^2 + \beta k_0 - 2\beta A^2(2\mu + \nu - i\sigma_R) - 1/4]k^4 \\ + [9\beta^2 k_0^4 - 6\beta k_0^3 + k_0^2(1 - 6\beta A^2(\mu + \nu - i\sigma_R)) \\ + k_0 A^2(\beta(6 - 6i\delta) + 3\mu + 2\nu - 2i\sigma_R) \\ + A^2(i\delta + \mu A^2(3\mu + 2\nu - 2i\sigma_R) - 1)]k^2,$$

and it should be recalled that $A^2 = -\gamma/\delta$. It is clear that the system will always be modulationally unstable, since the solutions of Eq. (B2) are in general complex.

-
- [1] M. J. Ablowitz and H. Segur, *Solitons and Inverse Scattering Transform* (SIAM, Philadelphia, 1981).
 [2] M. J. Ablowitz, *Nonlinear Dispersive Waves: Asymptotic Analysis and Solitons* (Cambridge University Press, Cambridge, UK, 2011).
 [3] A. Hasegawa and Y. Kodama, *Solitons in Optical Communications* (Oxford University Press, New York, 1996); G. P. Agrawal,

- Nonlinear Fiber Optics* (Academic Press, New York, 2012); Yu. S. Kivshar and G. P. Agrawal, *Optical Solitons: From Fibers to Photonic Crystals* (Academic Press, New York, 2003).
 [4] M. Scalora, M. S. Syrchin, N. Akozbek, E. Y. Poliakov, G. D'Aguzzo, N. Mattiucci, M. J. Bloemer, and A. M. Zheltikov, *Phys. Rev. Lett.* **95**, 013902 (2005); S. Wen, Y. Xiang, X. Dai, Z. Tang, W. Su, and D. Fan, *Phys. Rev. A* **75**, 033815 (2007);

- N. L. Tsitsas, N. Rompotis, I. Kourakis, P. G. Kevrekidis, and D. J. Frantzeskakis, *Phys. Rev. E* **79**, 037601 (2009).
- [5] R. S. Johnson, *Proc. R. Soc. Lond. A* **357**, 131 (1977).
- [6] Yu. V. Sedletsy, *J. Exp. Theor. Phys.* **97**, 180 (2003).
- [7] A. V. Slunyaev, *J. Exp. Theor. Phys.* **101**, 926 (2005).
- [8] N. N. Akhmediev and A. Ankiewicz, *Solitons. Nonlinear Pulses and Beams* (Chapman and Hall, London, 1997).
- [9] H. Haus, *IEEE J. Sel. Top. Quantum Electron.* **6**, 1173 (2000).
- [10] N. Akhmediev, J. M. Soto-Crespo, and G. Town, *Phys. Rev. E* **63**, 056602 (2001).
- [11] E. N. Tsoy and N. Akhmediev, *Phys. Lett. A* **343**, 417 (2005).
- [12] E. N. Tsoy, A. Ankiewicz, and N. Akhmediev, *Phys. Rev. E* **73**, 036621 (2006).
- [13] D. Sanvitto and V. Timofeev, *Exciton Polaritons in Microcavities* (Springer-Verlag, Berlin, 2012).
- [14] N. Akhmediev and A. Ankiewicz (eds.), *Dissipative Solitons* (Springer-Verlag, Berlin, 2005).
- [15] M. C. Cross and P. C. Hohenberg, *Rev. Mod. Phys.* **65**, 851 (1993); I. S. Aranson and L. Kramer, *ibid.* **74**, 99 (2002).
- [16] M. W. Hirsch, S. Smale, and R. L. Devaney, *Differential Equations, Dynamical Systems, and an Introduction to Chaos* (Elsevier, Amsterdam, 2004).
- [17] I. G. Kevrekidis, B. Nicolaenko, and J. C. Scovel, *SIAM J. Appl. Math.* **50**, 760 (1990); F. Christiansen, P. Cvitanović, and V. Putkaradze, *Nonlinearity* **10**, 55 (1997).
- [18] H. T. Moon, P. Huerre, and L. G. Redekopp, *Phys. Rev. Lett.* **49**, 458 (1982); K. Nozaki and N. Bekki, *ibid.* **51**, 2171 (1983); R. J. Deissler and H. R. Brand, *ibid.* **72**, 478 (1994).
- [19] K. Nozaki and N. Bekki, *Phys. Rev. Lett.* **50**, 1226 (1983); *Physica D* **21**, 381 (1986); *Phys. Lett. A* **102**, 383 (1984).
- [20] D. Cai, D. W. McLaughlin, and J. Shatah, *Phys. Lett. A* **253**, 280 (1999).
- [21] E. Shlizerman and V. Rom-Kedar, *Chaos* **15**, 013107 (2005); *Phys. Rev. Lett.* **96**, 024104 (2006); **102**, 033901 (2009).
- [22] Y. Li and D. W. McLaughlin, *Commun. Math. Phys.* **162**, 175 (1994); G. Haller and S. Wiggins, *Physica D* **85**, 311 (1995).
- [23] A. R. Bishop, K. Fesser, P. S. Lomdahl, W. C. Kerr, M. B. Williams, and S. E. Trullinger, *Phys. Rev. Lett.* **50**, 1095 (1983); A. R. Bishop, M. G. Forest, D. W. McLaughlin, and E. A. Overman, II, *Phys. Lett. A* **144**, 17 (1990); G. Kovačič and S. Wiggins, *Physica D* **57**, 185 (1992); N. Ercolani, M. G. Forest, and D. W. McLaughlin, *ibid.* **43**, 349 (1990).
- [24] H. Ikeda, M. Matsumoto, and A. Hasegawa, *Opt. Lett.* **20**, 1113 (1995).
- [25] T. P. Horikis and D. J. Frantzeskakis, *Opt. Lett.* **38**, 5098 (2013).
- [26] Y. Chen and J. Atai, *Opt. Lett.* **16**, 1933 (1991); Y. Chen, *Phys. Rev. A* **45**, 6922 (1992); Yu. S. Kivshar and X. Yang, *Phys. Rev. E* **49**, 1657 (1994).
- [27] S. C. V. Latas, M. F. S. Ferreira, and M. V. Facão, *Appl. Phys. B* **104**, 131 (2011); S. C. V. Latas and M. F. S. Ferreira, *Opt. Lett.* **37**, 3897 (2012); I. M. Uzunov, T. N. Arabadzhiev, and Z. D. Georgiev, *Opt. Fiber Tech.* **24**, 15 (2015).
- [28] F. Salin, P. Grangier, G. Roger, and A. Brun, *Phys. Rev. Lett.* **56**, 1132 (1986).
- [29] H. A. Haus, K. Tamura, L. E. Nelson, and E. P. Ippen, *IEEE J. Quantum Electron.* **31**, 591 (1995).
- [30] G. D. Van Wiggeren and R. Roy, *Science* **279**, 1198 (1998).
- [31] M. J. Ablowitz, S. D. Nixon, T. P. Horikis, and D. J. Frantzeskakis, *J. Phys. A* **246**, 095201 (2013).
- [32] V. Achilleos, S. Diamantidis, D. J. Frantzeskakis, T. P. Horikis, N. I. Karachalios, and P. G. Kevrekidis, *Physica D* **316**, 57 (2016).
- [33] V. E. Zakharov and L. A. Ostrovsky, *Physica D* **238**, 540 (2009).
- [34] T. B. Benjamin and J. E. Feir, *J. Fluid Mech.* **27**, 417 (1967).
- [35] K. Ikeda, H. Daido, and O. Akimoto, *Phys. Rev. Lett.* **45**, 709 (1980).
- [36] P. Cvitanović, R. L. Davidchack, and E. Siminos, *SIAM J. Appl. Dynam. Syst.* **9**, 1 (2010).
- [37] To obtain the equation, multiply Eq. (2) by u^* and its conjugate by u , add the equations, and integrate in $[-L, L]$ using the relevant boundary conditions.
- [38] R. Temam, *Infinite-Dimensional Dynamical Systems in Mechanics and Physics* (Springer-Verlag, Berlin, 1997).
- [39] M. J. Potasek, *Opt. Lett.* **12**, 921 (1987).